npj | Quantum Materials

www.nature.com/npjquantmats

ARTICLE OPEN

Direct observation of a uniaxial stress-driven Lifshitz transition in Sr_2RuO_4

Veronika Sunko[1,2], Edgar Abarca Morales[1,2], Igor Marković[1,2], Mark E. Barber[1], Dijana Milosavljević[1], Federico Mazzola[2], Dmitry A. Sokolov[1], Naoki Kikugawa[3], Cephise Cacho[4], Pavel Dudin[4], Helge Rosner[1], Clifford W. Hicks[1], Philip D. C. King[2] and Andrew P. Mackenzie[1,2]

Pressure represents a clean tuning parameter for traversing the complex phase diagrams of interacting electron systems, and as such has proved of key importance in the study of quantum materials. Application of controlled uniaxial pressure has recently been shown to more than double the transition temperature of the unconventional superconductor Sr_2RuO_4, leading to a pronounced peak in T_c versus strain whose origin is still under active debate. Here we develop a simple and compact method to passively apply large uniaxial pressures in restricted sample environments, and utilise this to study the evolution of the electronic structure of Sr_2RuO_4 using angle-resolved photoemission. We directly visualise how uniaxial stress drives a Lifshitz transition of the γ-band Fermi surface, pointing to the key role of strain-tuning its associated van Hove singularity to the Fermi level in mediating the peak in T_c. Our measurements provide stringent constraints for theoretical models of the strain-tuned electronic structure evolution of Sr_2RuO_4. More generally, our experimental approach opens the door to future studies of strain-tuned phase transitions not only using photoemission but also other experimental techniques where large pressure cells or piezoelectric-based devices may be difficult to implement.

npj Quantum Materials (2019)4:46 ; https://doi.org/10.1038/s41535-019-0185-9

INTRODUCTION

The layered perovskite Sr_2RuO_4 has been extensively studied both because of its celebrated unconventional superconductivity,[1–6] and the accuracy with which its normal state properties can be measured,[7–11] and analysed.[12–15] Its metallic state is strongly correlated, with mass renormalisations in the range 3–5, and it is proving to be a benchmark material for the development of correlated electron theory.[11,16] In spite of the understanding of the metallic state, and a quarter of a century of research, there is still no consensus on its superconducting order parameter symmetry or the mechanism by which the superconductivity condenses.[6] Indeed, a recent nuclear magnetic resonance Knight shift measurement has ruled out the previously most-favoured triplet order parameter and opened a host of alternative possibilities.[17] This is a major unsolved problem because the electronic structure of Sr_2RuO_4 is relatively simple compared with that of many other unconventional superconductors, and its metallic state, though strongly correlated, is firmly established to be a Fermi liquid below ~30 K.[8] Furthermore, its superconductivity is closer to the weak-coupling limit than in any other unconventional superconductor, as evidenced by its mean-field-like heat capacity anomaly.[18–20] In short, the Sr_2RuO_4 problem is one that should be soluble, and understanding it fully is therefore a benchmark for the progress of the fields of strongly interacting systems and unconventional superconductivity.

Recent years have seen the development of uniaxial pressure as a new probe of the physics of Sr_2RuO_4.[21–24] Unlike most unconventional superconductors, Sr_2RuO_4 has a long superconducting coherence length of over 70 nm, a further consequence of its weak-coupling superconductivity. This in turn renders the superconducting condensate the most sensitive to disorder of any known superconductor; the mean free path must be ~1 μm or larger for the superconductivity to be studied in the clean limit.[25] Any external tuning of the superconducting state must therefore preserve this extremely long mean free path, a constraint that has led to the failure of attempts to study the superconductivity while tuning the density of states at the Fermi level by chemical doping[26] or the application of biaxial epitaxial strain to thin films.[27] These issues can be overcome by the application of uniaxial pressure to high purity single crystals,[21,23,24] which has been shown to raise T_c from 1.5 to 3.5 K, and explain observations of inhomogeneous traces of 3 K superconductivity as being due to strain gradients, either externally imposed strain inhomogeneneity[28] or around Ru inclusions in eutectic crystalline Ru–Sr_2RuO_4 mixtures.[29]

If the Fermi level of a material sits near a so-called van Hove singularity in which the dispersion has a saddle point and the density of states diverges, it is possible in principle to tune across that saddle point, changing the Fermi surface topology in what is often referred to as a Lifshitz transition.[30] Based on density-functional calculations,[23] as well as previous spectroscopic work which has identified the position of a van Hove singularity 14 meV above the Fermi level at the M point of the Brillouin zone,[26,27] a working hypothesis has been that uniaxial pressure is driving the so-called γ Fermi surface sheet of Sr_2RuO_4 through such a Lifshitz transition.[23,24,31] In this picture, the superconductivity is enhanced primarily by the resulting maximum in the density of states.

[1]Max Planck Institute for Chemical Physics of Solids, Nöthnitzer Strasse 40, 01187 Dresden, Germany; [2]SUPA, School of Physics and Astronomy, University of St. Andrews, St. Andrews KY16 9SS, UK; [3]National Institute for Materials Science, Tsukuba, Ibaraki 305-0003, Japan and [4]Diamond Light Source, Harwell Campus, Didcot OX11 0DE, UK
Correspondence: Clifford W. Hicks (Clifford.Hicks@cpfs.mpg.de) or Philip D. C. King (philip.king@st-andrews.ac.uk) or Andrew P. Mackenzie (Andy.Mackenzie@cpfs.mpg.de)

Received: 1 July 2019 Accepted: 19 July 2019
Published online: 19 August 2019

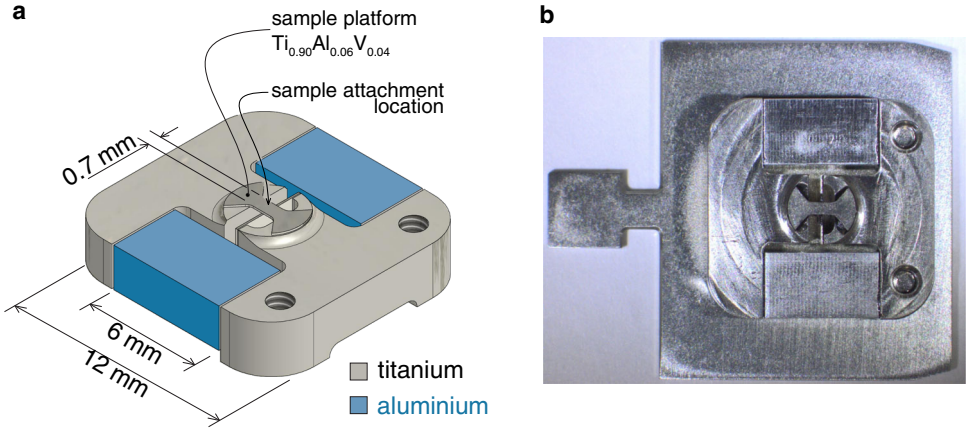

Fig. 1 Differential thermal contraction strain rig. **a** An illustration of the strain rig. The thermal contraction of aluminium exceeds that of titanium, leading to uniaxial compression of the sample platform during cooling. There is a copy of this platform on the underside, to maintain symmetry and avoid bending under the thermal stresses. Different parts of the device are joined by Stycast 2850. **b** A photograph of the strain rig mounted on a standard flag-style sample plate

However, it remains unclear if the intuitions based on single particle calculations really represent a good starting point for considering strain-dependent changes to a Hund's metal system where orbital-dependent correlations are known to be highly important.[11,32] Indeed, it has been predicted that strain may alternatively trigger an intervening phase, such as a spin-density wave, which cuts off an increase in T_c before the Lifshitz transition is reached.[33] It is thus crucial to obtain direct, *k*-resolved spectroscopic evidence for the electronic structure evolution that is taking place over a comparable strain range for which T_c is known to peak.

In principle, angle-resolved photoemission spectroscopy (ARPES) is an ideal tool for this purpose, but this kind of experiment presents severe experimental challenges. Using piezoelectric-driven uniaxial pressure cells, as in,[21–24] would require major re-engineering of conventional ARPES manipulators and careful shielding. For compatibility with present facilities, our goal here was to develop a sample stage that fits onto standard sample carriers, implying maximum dimensions of ca. $12 \times 12 \times 3\ mm^3$. In addition, to study single crystals it must be possible to cleave samples mounted on the apparatus. For ARPES measurements, large strains have been applied to low-elastic-modulus materials,[34] and spring- and piezo-based devices have been used for detwinning.[35–38] In ref. [39] a bending mechanism was employed to apply large adjustments to the strain of a sample placed under strong uniaxial compression by its unusual thermal contraction. However, it has proved difficult to realise large strains in high-elastic-modulus materials in a general way. Indeed, in our first attempt using a spring-based rig driven by an adjustment screw actuated *ex-situ* (described in the Supplementary Information, Fig. S1), we could not achieve a uniaxial stress in Sr_2RuO_4 larger than its room-temperature elastic limit of ~0.2 GPa, well below the value required to reach the peak in T_c.[40] In this paper, we report a new experimental design that uses differential thermal contraction[41] to apply uniaxial stress gradually as the sample is cooled, and use it to successfully obtain ARPES data on Sr_2RuO_4 driven across its Lifshitz transition. In doing so we clarify the physics of this important correlated metal and superconductor, and demonstrate a technology that we believe will prove extremely useful for the study of a wide range of other materials.

RESULTS

Our custom strain rig is illustrated in Fig. 1a. Details of its design and operation are given in Methods; here we state the key point which is that differential thermal contraction of the Ti and Al support blocks delivers, upon cooling from room temperature to below ~40 K, a uniaxial compression of 0.6% (see Methods) to a sample platform in which there is excellent strain field homogeneity. Taking into account the Poisson's ratio of titanium, this yields an anisotropic strain ε_{xx}–ε_{yy} of −0.8%, where ε_{xx} is the longitudinal strain in the platform, ε_{yy} the transverse strain, and negative values denote compression. We have confirmed that such an anisotropic strain is achieved through comparison of optical micrographs measured at room temperature and ~10 K (Supplemental Fig. S2). The whole assembly fits comfortably on a standard flag-style sample plate (Fig. 1b), of the form commonly found in ultra-high vacuum-based techniques such as ARPES or scanning probe methods. The sample, mounted on top of the platform, remains fully accessible for e.g. sample cleaving and subsequent measurement.

In Fig. 2 we show two example data sets, from the extremes of strain reached in the experiment. For an unstrained sample mounted on a conventional sample plate (Fig. 2b), the three-known bulk bands of Sr_2RuO_4 are clearly seen, with no signs of surface states (see 'Methods' section). The large, nearly circular γ sheet closes around Γ as an electron pocket, in agreement with a large number of previous measurements.[9–11,27] The data shown in Fig. 2d are from a sample for which an anisotropic strain of $\varepsilon_{xx} - \varepsilon_{yy} = -0.7 \pm 0.1\%$ was achieved, as determined by optical characterisation (see Fig. S2 of the Supplementary Information). In sharp contrast to the unstrained case, the γ sheet is no longer a circle but an open sheet along the *y* axis. This is in agreement with the calculations of how the Fermi surface of Sr_2RuO_4 would look after traversal of its van Hove singularity (vHs) located at $(0, \pm\pi)$.[23,33,42]

Confirmation that the vHs has indeed been traversed comes from inspection of the dispersions measured along the Γ-M_1 and Γ-M_2 directions (in the strained sample, we distinguish between the M points located at $(\pm\pi,0)$ and $(0,\pm\pi)$, denoting these as M_1 and M_2, respectively). For Γ-M_1 (Fig. 3a) the Fermi surface crossings of both the β and γ sheets are clearly visible, but along Γ-M_2 (Fig. 3b) the top of the γ-band lies below the Fermi level. As seen in Fig.

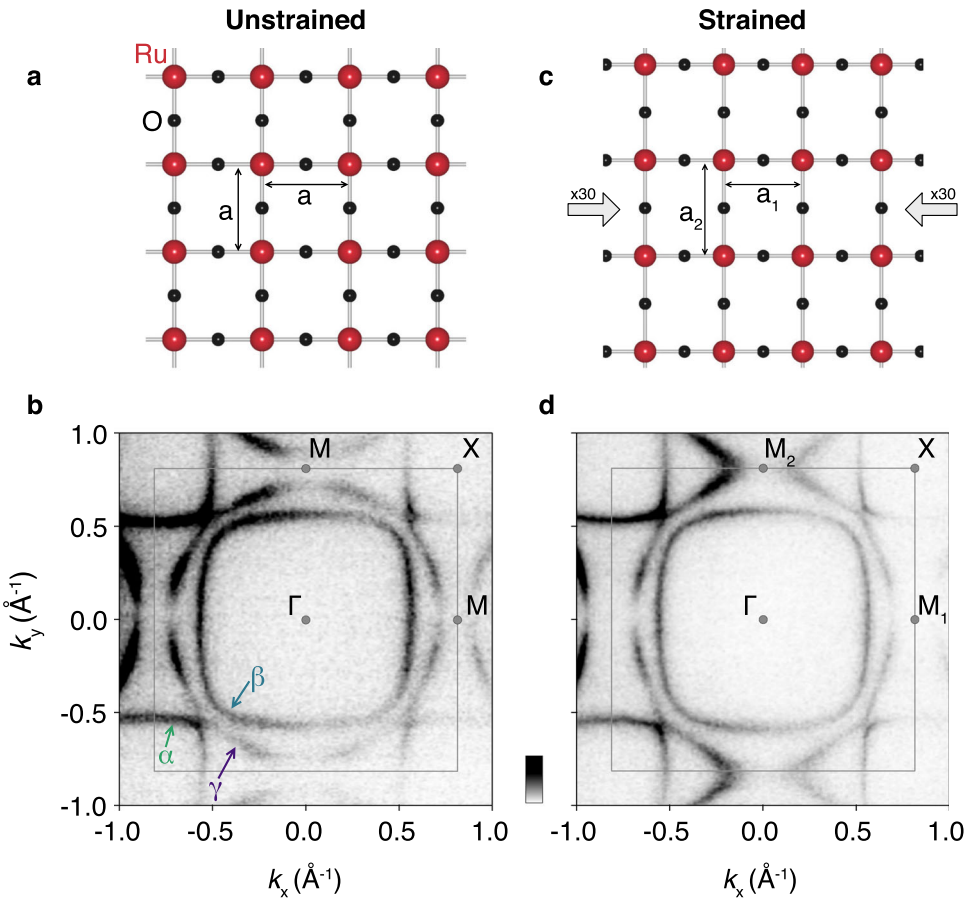

Fig. 2 Strain-driven Lifshitz transition in Sr_2RuO_4. **a** Schematic of the RuO_2 plane of Sr_2RuO_4, in its unstrained tetragonal phase. **b** ARPES measurements of the corresponding Fermi surface show the expected C_4 symmetry, with clear observation of the square hole pockets (α) located at the Brillouin zone corners and large nearly square (β) and circular (γ) electron-like pockets located at the zone centre. **c** Exaggerated (by a factor of 30) distortion of the RuO_2 plane by application of a uniaxial stress along [100], leading to an anisotropic strain of 0.7%. **d** A large distortion of the γ Fermi surface is immediately apparent, causing it to become open along k_y, consistent with having traversed a van Hove singularity at M_2

3c, the combined Γ-M_2 − X cut reveals that this band displays the basic topography of the simple zone edge vHs predicted by band theory and sketched in Fig. 3d: the dispersion rises along Γ-M_2, then flattens at the saddle point and then rises slightly along M_2 − X before the data are cut off by the Fermi function.

The data in Figs. 2 and 3 firmly establish the qualitative result that we have been able to achieve a high enough uniaxial pressure to drive Sr_2RuO_4 through its Lifshitz transition at the M_2 point of the Brillouin zone. Moreover, the anisotropic strain for which we achieve this is in agreement within experimental error with that required[24,40] to reach a peak in the superconducting T_c, and at which the low-temperature resistivity deviates from a T^2 temperature-dependence (for details see Supplementary Fig. S2). This therefore provides compelling evidence that both are directly driven by tuning of the γ-band vHS to the Fermi level, a scenario also supported by analysis of the superconducting critical field,[23] and NMR Knight shift[31] data.

It is desirable to track the strain evolution of the Fermi surface approaching this van Hove singularity. Although our strain device based on thermal contraction is not inherently tuneable without changing the temperature, it is in fact possible to achieve a range of sample strains at low temperature by varying the sample thickness (see 'Methods' section). It is thus highly beneficial to have an internal measure of the strain achieved in every sample. Analysis of the β sheet provides such a metric. The band topography makes its distortion much smaller than that of the γ sheet; indeed it is hardly visible simply by looking at Fig. 2d. However, it exists, and can be traced by fitting momentum distribution curves extracted radially around the Fermi surface (dots in Fig. 4a). As shown in Fig. 4b, this analysis reveals how the β sheet k_F along the Γ-M_1 and Γ-M_2 directions differ by 0.025Å^{-1} in the highly strained sample (Fig. 2d, reproduced with fits in Fig. 4a). This difference corresponds to an asymmetry, $(k_F(\Gamma\text{-}M_2) - k_F(\Gamma\text{-}M_1))/(k_F(\Gamma\text{-}M_2) + k_F(\Gamma\text{-}M_1))$, of ~2%. This small change means that the β sheet distortion is likely in the linear response regime to a good approximation, so that the measured anisotropy can be used as a linear scale of the microscopic strain in every sample. The much larger γ sheet anisotropy is shown in an equivalent plot in Fig. 4c.

Making use of the above-described β-band asymmetry, we show in Fig. 5a the strain dependence of the γ sheet M point anisotropy for five samples subjected to varying uniaxial stress

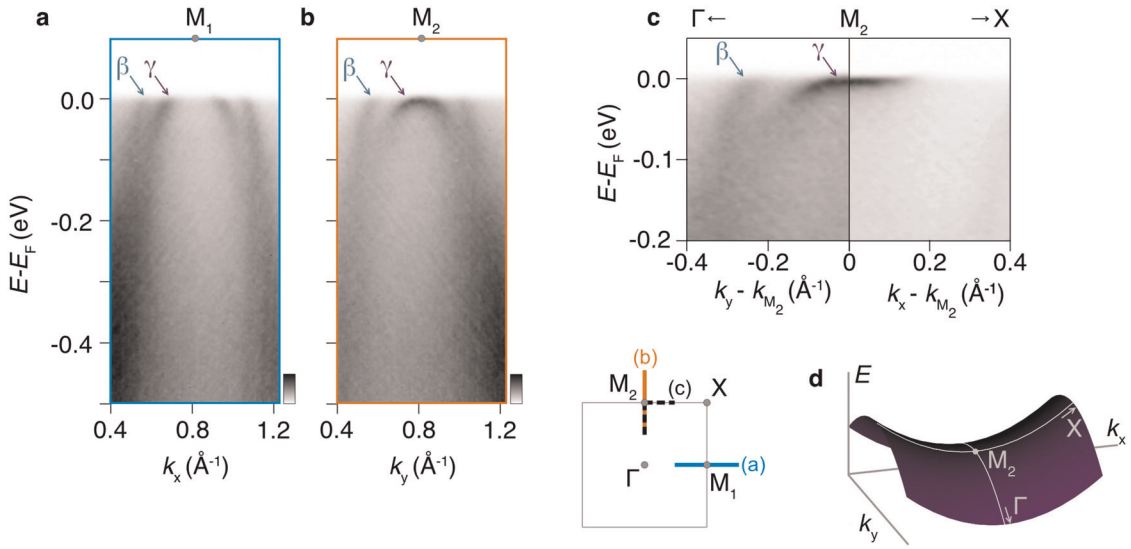

Fig. 3 Strain-tuning to the van Hove singularity. **a**, **b** Dispersions of Sr_2RuO_4 under anisotropic strain in the vicinity of the Brillouin zone boundary, measured along the **a** Γ-M_1 and **b** Γ-M_2 directions (see inset). The γ-band is clearly located above E_F at the M_1 point, intersecting the Fermi level away from M_1 along the Γ-M_1 direction. In contrast, the γ-band is pushed below the Fermi level at M_2, with a fully-occupied parabolic band visible along Γ-M_2. **c** Measurements along the orthogonal directions away from M_2 (see inset) reveal the saddle point nature of the band dispersion at the M points, with a barely-occupied upward dispersing band visible along M_2-X before it is cut off by the Fermi function. The saddle point is shown schematically in **d**

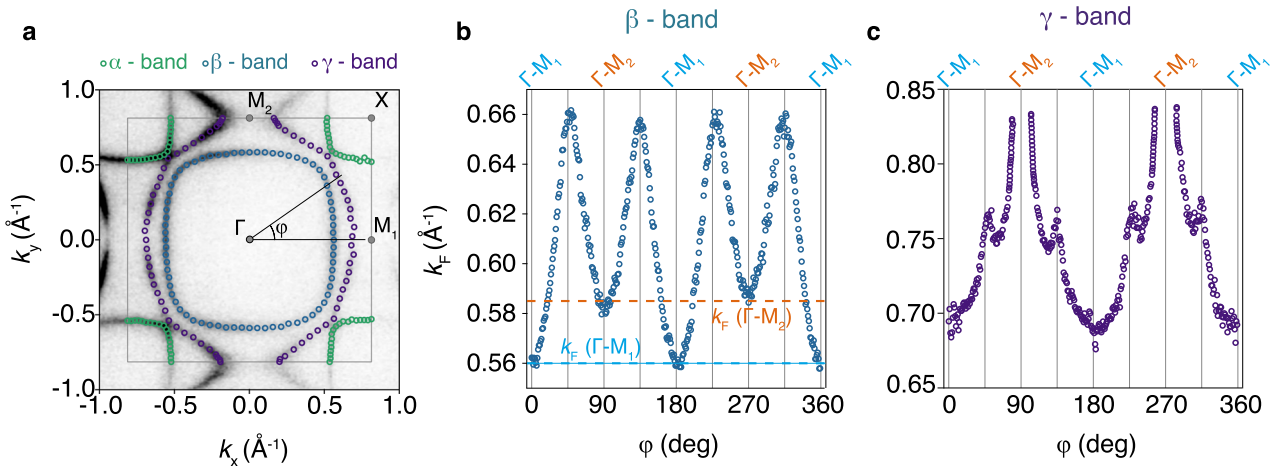

Fig. 4 Quantitative analysis of Fermi surface anisotropy. **a** Fermi surface of uniaxially-pressured Sr_2RuO_4 (image plot) with Fermi momenta (points) extracted from fitting MDCs. **b**, **c** Corresponding k_F of the **b** β- and **c** γ-band Fermi surfaces as a function of radial angle, φ (see **a**) A small C_2 distortion of the β-sheet Fermi surface is evident, while the γ-sheet develops open contours

(see Supplementary Fig. S3), including one pressurised with our original spring-based rig (see Supplementary Fig. S1). We parameterise the γ sheet distortions via the momentum separation of the γ Fermi surfaces in neighbouring Brillouin zones or, when its Fermi contour becomes open, by the momentum separation between the two branches along the Brillouin zone boundary. We define the latter as negative, to reflect its distinct topology. At M_1, $\Delta k_{F,M1}$ grows monotonically with increasing strain, reflecting an upwards shift of the vHs at this point, and hence reduction in k_F of the γ-barrel along Γ-M_1. This is driven by the greater overlap of d_{xy} orbitals along this compressively strained direction. Along Γ-M_2, a tensile strain is induced due to the positive Poisson's ratio of the sample platform, and the γ-band bandwidth consequently narrows, causing the vHs to drop below E_F along this direction. $\Delta k_{F,M2}$ therefore reduces, and changes sign as the vHs is traversed.

This behaviour is qualitatively reproduced in the Fermi surface topology as calculated by relativistic density functional theory (DFT) (Fig. 5b, c). However, to investigate whether this single particle calculation correctly captures the strain-dependent Fermi surface evolution, a more quantitative comparison is needed. Here we again make use of the β-band asymmetry as an internal reference of the anisotropic strain. Indeed, our calculations (Supplementary Fig. S4a) confirm that the β-band asymmetry is linearly proportional to the asymmetric strain. Moreover, they show that this metric is independent of the Poisson's ratio used in the calculation, providing an elegant way to compare results for samples mounted on platforms with freestanding samples, as, for example, investigated in refs. [21,23,24,40]

Our calculations provide an excellent match to the measured strain evolution of the γ Fermi surface in the vicinity of the M_1 point (Fig. 5a). Close to M_2, however, the agreement becomes much poorer as the Lifshitz transition is approached. The

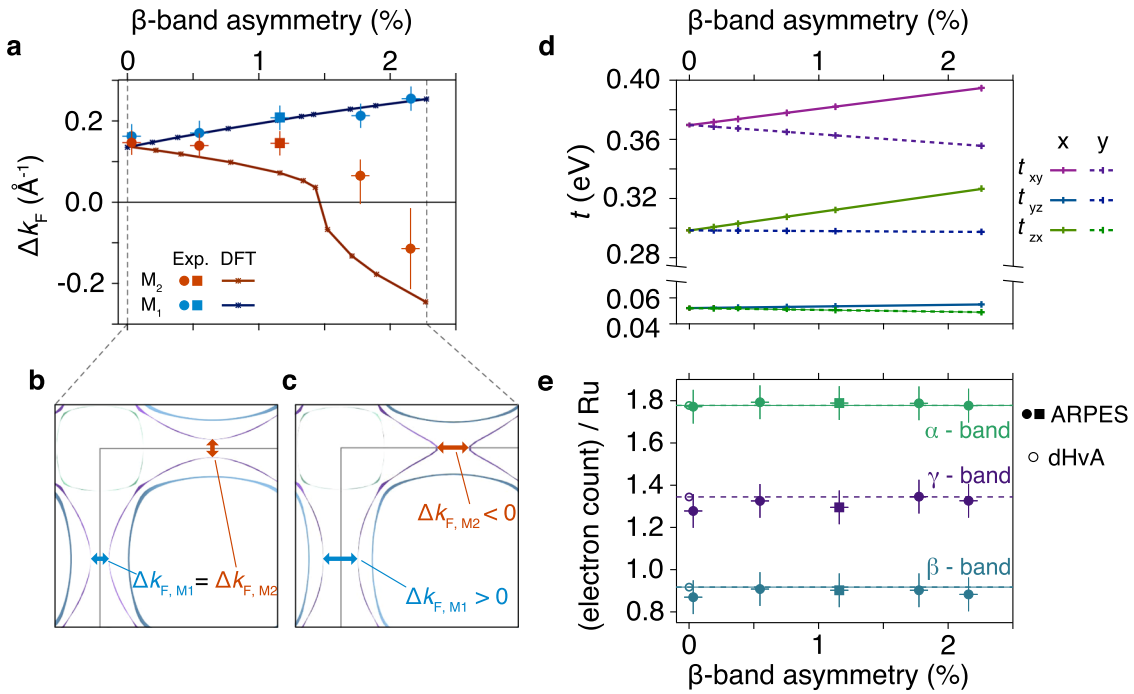

Fig. 5 Strain evolution of Fermi surface anisotropy. **a** Parametrization of the γ-sheet anisotropy, encoded via the momentum separation of γ Fermi surfaces in neighbouring Brillouin zones ($\Delta k_F > 0$) or by the momentum separation between the two branches along the Brillouin zone boundary once the Fermi contour becomes open ($\Delta k_F < 0$). These are plotted as a function of anisotropic strain encoded via the β-sheet asymmetry. The square symbols are from a sample mounted on the spring-based rig described in the Supplementary Information (Fig. S1). The measured Fermi surfaces and dispersions from all of the samples included here are shown in Supplementary Fig. S3. Calculated Fermi surfaces for unstrained (**b**) and strained (**c**) Sr_2RuO_4. The line thickness encodes the degree of out-of-plane dispersion. **d** Downfolding the calculations onto a basis of Ru-centered Wannier functions representing the Ru 4*d xy*, *xz* and *yz* orbitals, we find that the hopping terms, shown here for nearest neighbours, vary linearly with strain with orbital-dependent prefactors. **e** Strain-dependent measurements of the Luttinger counts of the three Fermi surfaces, showing no resolvable changes as a function of strain

discrepancy between the DFT and the experiment is larger than the uncertainties associated with either (see also Supplementary Fig. S4b), likely reflecting a many-body contribution (see also ref. [31,43]). At the single particle level, our DFT calculations downfolded on a Wannier tight-binding basis (see 'Methods' section) predict a linear scaling of the hopping parameters with strain (Fig. 5d), with orbital-dependent pre-factors.

DISCUSSION

It is an interesting open question whether the discrepancies between the strain evolution of the Fermi surface predicted by the linear scaling described above and that found in our measurements can be understood on the basis of local self-energies, as in unstrained Sr_2RuO_4,[11] or may in fact imply that correlations become momentum-dependent in the vicinity of the Lifshitz transition. Spectroscopic study in this range of strains is particularly desirable because of the potential consequences of van Hove singularities in producing transport and susceptibility power laws that do not conform with the expectations for a standard Fermi liquid.[24,31,44–47] This is an area of strong and growing interest, and one in which the tunability of Sr_2RuO_4 will play an important role.

Our findings therefore motivate future theoretical work studying the strain evolution of electronic correlations in Sr_2RuO_4, as well as providing important constraints for such studies. For example, we find that the Luttinger counts of each of the α-, β- and γ-band Fermi surfaces (Fig. 5e) is, within our experimental uncertainty, independent of strain and consistent with the values known from de Haas van Alphen measurements in unstrained Sr_2RuO_4.[8] This is in contrast to the case of biaxial epitaxial strain,[27] for which approaching the vHs in Sr_2RuO_4 relies on a redistribution of charge carrier density between the α-, β- and γ-bands. The data in Fig. 5e indicate that uniaxial pressure tuning to the van Hove singularity instead results essentially entirely from distortion of the γ-band.

The results presented in this paper represent the first *k*-resolved spectroscopic evidence for the uniaxial stress-driven changes in the electronic structure of Sr_2RuO_4. Within experimental error, the strain at which ARPES shows that the van Hove singularity in the γ sheet is reached is the same as the narrow range of strains at which there are strong peaks in T_c, the normal state NMR Knight shift and normal state resistivity. Our findings therefore provide strong evidence that, as previously postulated but not proven, all of these phenomena are associated with the Lifshitz transition caused by traversing this van Hove singularity. This has important implications for understanding the normal state and superconducting physics of Sr_2RuO_4, and offers the prospect of testing modern theories of its electronic structure and superconducting instability. Crucially, such investigations are made experimentally feasible by our basic passive platform design, which can easily be incorporated in laser-based systems, yielding the best energy and momentum resolution available to modern angle-resolved photoemission. What is more, the minimalistic and compact design of our device will allow it to be used in other extreme environments, without the need to construct a bespoke instrument for every application. This simple approach is ideal for exploration of the large parameter space that can be used for tuning of quantum materials, and we believe could lead to discoveries of novel phases and effects in a wide range of compounds.

METHODS

Differential thermal contraction strain rig

We describe here the design and operation of our uniaxial stress apparatus shown in Fig. 1. This stage uses the differential thermal contraction between aluminium and titanium to uniaxially compress a sample platform. Aluminium contracts by 0.42% between room temperature and the measurement temperature, and titanium by 0.15%. This differential contraction is applied over a length of 6 mm, producing a thermal displacement of 16 μm. By necking the sample platform, its spring constant can be kept low relative to those of the other components, so that the resulting elastic deformation is concentrated into the neck. The spring constant of the two platforms together (there is a mirror of the sample platform on the bottom, to keep the device symmetric) is ≈8 N/μm. That of the remaining parts of the device, meaning the aluminium struts and titanium bars that generate the thermal displacement, is ≈20 N/μm, so $20/(20+8) \approx 70\%$ of the thermal displacement goes into the platforms. This compresses them uniaxially by ~0.6% between room temperature and below ~40 K, resulting in an anisotropic strain in the platform of $|\varepsilon_{xx} - \varepsilon_{yy}| \approx 0.8\%$. This value is confirmed by comparison of optical micrographs taken at room temperature and 10 K (Supplementary Fig. S2). Crucially, this strain is applied gradually as the sample is cooled: the elastic limit of single-crystal Sr_2RuO_4 is as low as 0.15% at room temperature but at least 1% at 5 K,[40] and by making use of differential thermal contraction in this way strain is applied to the sample as its elastic limit increases with cooling.

The sample is affixed to the necked portion of this platform using silver epoxy; this is the conventional sample mounting approach for ARPES measurements. Although this stage is not intrinsically tunable, the strain achieved in the sample varies with sample thickness, allowing different strains to be realised from different cleaves. This was most likely achieved through a combination of elastic and nonelastic deformation of the epoxy. The samples were in a size range permitting, even with fully elastic epoxy deformation, partial strain transmission. The datasheet for Epotek H21D silver epoxy indicates a room-temperature storage modulus, equivalent to the Young's modulus for elastic materials, of 5.5 GPa, while the Young's modulus for stress along a Ru–Ru bond direction in Sr_2RuO_4 is ~176 GPa.[48] This large difference in Young's moduli means that the strain in the sample locks to that in the platform over a length scale λ that increases as the sample is made thicker. For epoxy and sample thicknesses both on the order of 10 μm, this length scale λ = ~100 μm. Our samples were typically ~600 μm across, larger but not drastically larger than λ, allowing meaningful variation in the achieved sample strain through varying sample thickness. Epoxy creep at higher temperatures is likely to have provided an additional mechanism to relax strain,[49] which would also be more effective for thicker samples. Samples were cleaved at room temperature, so for cooling the sample stage from the epoxy curing temperature of 120 °C to room temperature the samples were thicker—generally 50–150 μm thick—and so also mechanically stronger than during cooling from room temperature.

Angle-resolved photoemission

High-quality single-crystal Sr_2RuO_4 samples were grown in a floating zone furnace (Canon Machinery) using techniques refined over many years to those described recently in ref. [50] These were cut into square platelets of dimensions ca. 600×600 μm^2 with the square edge oriented along [100] and, except where stated, were mounted on the custom sample stage shown in Fig. 1, with the [100] direction aligned to the uniaxial compression direction of the strain cell. The samples had varying thickness down to ca. 15 μm (Supplementary Fig. S2), enabling different strains to be achieved as discussed above. ARPES measurements were performed at the I05 beamline of Diamond Light Source,[51] at a manipulator temperature of ~10 K. We used 68 eV linear horizontal (LH, *p*-polarised) photons for Fermi surface maps, 40 eV LH photons for measurements of the Γ-M dispersions, and 40 eV linear vertical (*s*-pol) light for measurement of the M–X dispersion, all chosen to ensure the most favourable transition matrix elements.

In situ cleaved Sr_2RuO_4 is known to support surface states which substantially complicate the measured spectra in unstrained Sr_2RuO_4.[9] It would be difficult to separate the strain-induced changes of the bulk electronic structure from the surface contributions. We therefore cleaved our samples in air immediately prior to loading them into the vacuum chamber. The resulting ARPES measurements of an unstrained reference sample mounted on a standard sample plate (Fig. 2(a)) reveal only the three well-known bulk Fermi surfaces of Sr_2RuO_4,[2] with no observable trace of surface-derived features. We therefore proceeded with this method for all of our measurements of strained Sr_2RuO_4.

Density-functional theory

DFT electronic structure calculations were performed using the full-potential local orbital FPLO code,[52,53] version fplo18.00-52 (http://www.fplo.de). For the exchange-correlation potential, within the local density approximation the parametrizations of Perdew–Wang[54] was chosen. The spin–orbit (SO) coupling was treated non-perturbatively solving the four component Kohn–Sham–Dirac equation.[55] To obtain precise band structure and Fermi surface information, the final calculations were carried out on a well-converged mesh of 64.000 *k*-points ($40 \times 40 \times 40$ mesh, 8631 points in the irreducible wedge of the Brillouin zone). As starting point, for the unstrained crystal structure the structural parameters from ref. [56] at 15K have been used. Except where stated, the room-temperature experimental Poisson ratio was used for the calculations at finite strain with the free internal structural parameters optimised, minimising forces below 1 meV/Å. A three band tight-binding model was constructed from Ru-centered Wannier functions for the 4*d xy*, *xz* and *yz* orbitals.

DATA AVAILABILITY

The research data supporting this publication can be accessed at https://doi.org/10.17630/3e6129ea-441a-486c-be5c-23a812c93cd2.

ACKNOWLEDGEMENTS

We thank T. Kim and M. Watson for useful discussions, and U. Nitzsche (IFW Dresden) for support with computational facilities. We gratefully acknowledge support from the European Research Council (Grant no. ERC-714193-QUESTDO), the Royal Society, the Max-Planck Society and the International Max-Planck Partnership for Measurement and Observation at the Quantum Limit. V.S. acknowledges EPSRC for PhD studentship support through grant number EP/L015110/1. E.A.M. and I.M. acknowledge PhD studentship support from the IMPRS for the Chemistry and Physics of Quantum Materials. N.K. acknowledges the support from JSPS KAKENHI (Nos. JP17H06136 and JP18K04715) and JST-Mirai Programme (No. JPMJMI18A3) in Japan. We thank Diamond Light Source for access to beamline I05 (Proposal no. SI20427), which contributed to the results presented here.

AUTHOR CONTRIBUTIONS

V.S., E.A.M., I.M., F.M. and P.D.C.K. performed the photoemission measurements, which were analysed by E.A.M., I.M. and V.S. C.W.H., V.S. and E.A.M. designed and assembled the uniaxial pressure apparatus. M.B. and E.A.M. characterised the rig and performed the optical image analysis. D.M. and H.R. performed the DFT calculations, and N.K. and D.A.S. grew the single crystals. C.C. and P.D. maintained the ARPES beamline and provided support. A.P.M. and P.D.C.K. led the project and wrote the paper with V.S., with input and comments from all co-authors.

ADDITIONAL INFORMATION

Supplementary Information accompanies the paper on the *npj Quantum Materials* website (https://doi.org/10.1038/s41535-019-0185-9).

Competing interests: The authors declare no competing interests.

Publisher's note: Springer Nature remains neutral with regard to jurisdictional claims in published maps and institutional affiliations.

REFERENCES

1. Maeno, Y. et al. Superconductivity in a layered perovskite without copper. *Nature* **372**, 532–534 (1994).
2. Mackenzie, A. P. & Maeno, Y. The superconductivity of Sr_2RuO_4 and the physics of spin-triplet pairing. *Rev. Mod. Phys.* **75**, 657–712 (2003).
3. Kallin, C. Chiral p-wave order in Sr_2RuO_4. *Rep. Prog. Phys.* **75**, 42501 (2012).
4. Maeno, Y., Kittaka, S., Nomura, T., Yonezawa, S. & Ishida, K. Evaluation of Spin-triplet Superconductivity in Sr_2RuO_4. *J. Phys. Soc. Jpn.* **81**, 11009 (2012).
5. Liu, Y. & Mao, Z.-Q. Unconventional superconductivity in Sr_2RuO_4. *Phys. C Supercond. Appl.* **514**, 339–353 (2015).
6. Mackenzie, A. P., Scaffidi, T., Hicks, C. W. & Maeno, Y. Even odder after twenty-three years: the superconducting order parameter puzzle of Sr_2RuO_4. *Npj Quantum. Mater.* **2**, 40 (2017).

7. Mackenzie, A. P. et al. Quantum oscillations in the layered perovskite superconductor Sr_2RuO_4. *Phys. Rev. Lett.* **76**, 3786–3789 (1996).
8. Bergemann, C., Mackenzie, A. P., Julian, S. R., Forsythe, D. & Ohmichi, E. Quasi-two-dimensional Fermi liquid properties of the unconventional superconductor Sr_2RuO_4. *Adv. Phys.* **52**, 639–725 (2003).
9. Damascelli, A. et al. Fermi surface, surface states, and surface reconstruction in Sr_2RuO_4. *Phys. Rev. Lett.* **85**, 5194–5197 (2000).
10. Veenstra, C. N. et al. Spin-orbital entanglement and the breakdown of singlets and triplets in Sr_2RuO_4 revealed by spin- and angle-resolved photoemission spectroscopy. *Phys. Rev. Lett.* **112**, 127002 (2014).
11. Tamai, A. et al. High-resolution photoemission on Sr_2RuO_4 reveals correlation-enhanced effective spin–orbit coupling and dominantly local self-energies. *Phys. Rev. X* **9**, 021048 (2019).
12. Nomura, T. & Yamada, K. Roles of electron correlations in the spin-triplet superconductivity of Sr_2RuO_4. *J. Phys. Soc. Jpn.* **71**, 1993–2004 (2002).
13. Raghu, S., Kapitulnik, A. & Kivelson, S. A. Hidden quasi-one-dimensional superconductivity in Sr_2RuO_4. *Phys. Rev. Lett.* **105**, 136401 (2010).
14. Scaffidi, T., Romers, J. C. & Simon, S. H. Pairing symmetry and dominant band in Sr_2RuO_4. *Phys. Rev. B* **89**, 220510 (2014).
15. Mravlje, J. et al. Coherence-incoherence crossover and the mass-renormalization puzzles in Sr_2RuO_4. *Phys. Rev. Lett.* **106**, 096401 (2011).
16. Zingl, M., Mravlje, J., Aichhorn, M., Parcollet, O. & Georges, A. Sign changes of the Hall coefficient in Sr_2RuO_4 reveal coherent-to-incoherent and elastic-to-inelastic crossovers. *ArXiv Prepr*. https://arxiv.org/abs/190205503 (2019).
17. Pustogow, A. et al. Pronounced drop of ^{17}O NMR Knight shift in superconducting state of Sr_2RuO_4. *ArXiv Prepr*. https://arxiv.org/abs/190400047 (2019).
18. Deguchi, K., Mao, Z. Q. & Maeno, Y. Determination of the superconducting gap structure in all bands of the spin-triplet superconductor Sr_2RuO_4. *J. Phys. Soc. Jpn.* **73**, 1313–1321 (2004).
19. Firmo, I. A. et al. Evidence from tunneling spectroscopy for a quasi-one-dimensional origin of superconductivity in Sr_2RuO_4. *Phys. Rev. B* **88**, 134521 (2013).
20. Kittaka, S. et al. Searching for gap zeros in Sr_2RuO_4 via field-angle-dependent specific-heat measurement. *J. Phys. Soc. Jpn.* **87**, 93703 (2018).
21. Hicks, C. W. et al. Strong Increase of T_c of Sr_2RuO_4 under both tensile and compressive strain. *Science* **344**, 283–285 (2014).
22. Hicks, C. W., Barber, M. E., Edkins, S. D., Brodsky, D. O. & Mackenzie, A. P. Piezoelectric-based apparatus for strain tuning. *Rev. Sci. Instrum.* **85**, 65003 (2014).
23. Steppke, A. et al. Strong peak in T_c of Sr_2RuO_4 under uniaxial pressure. *Science* **355**, eaaf9398 (2017).
24. Barber, M. E., Gibbs, A. S., Maeno, Y., Mackenzie, A. P. & Hicks, C. W. Resistivity in the vicinity of a van hove singularity: Sr_2RuO_4 under uniaxial pressure. *Phys. Rev. Lett.* **120**, (2018).
25. Mackenzie, A. P. et al. Extremely strong dependence of superconductivity on disorder in Sr_2RuO_4. *Phys. Rev. Lett.* **80**, 161–164 (1998).
26. Shen, K. M. et al. Evolution of the fermi surface and quasiparticle renormalization through a van hove singularity in $Sr_{2-y}La_yRuO_4$. *Phys. Rev. Lett.* **99**, 187001 (2007).
27. Burganov, B. et al. Strain control of fermiology and many-body interactions in two-dimensional ruthenates. *Phys. Rev. Lett.* **116**, 197003 (2016).
28. Taniguchi, H., Nishimura, K., Goh, S. K., Yonezawa, S. & Maeno, Y. Higher-T_c superconducting phase in Sr_2RuO_4 induced by in-plane uniaxial pressure. *J. Phys. Soc. Jpn.* **84**, 14707 (2015).
29. Maeno, Y. et al. Enhancement of superconductivity of Sr_2RuO_4 to 3 K by embedded metallic microdomains. *Phys. Rev. Lett.* **81**, 3765–3768 (1998).
30. Lifshitz, I. Anomalies of electron characteristics of a metal in the high pressure region. *Sov. Phys. Jetp-Ussr* **11**, 1130–1135 (1960).
31. Luo, Y. et al. Normal state ^{17}O NMR studies of Sr_2RuO_4 under uniaxial stress. *Phys. Rev. X* **9**, 021044 (2019).
32. Georges, A., de' Medici, L. & Mravlje, J. Strong correlations from Hund's coupling. *Annu. Rev. Condens. Matter Phys.* **4**, 137–178 (2013).
33. Liu, Y.-C., Zhang, F.-C., Rice, T. M. & Wang, Q.-H. Theory of the evolution of superconductivity in Sr_2RuO_4 under anisotropic strain. *Npj Quantum Mater.* **2**, (2017).
34. Flötotto, D. et al. In situ strain tuning of the dirac surface states in Bi_2Se_3 films. *Nano Lett.* **18**, 5628–5632 (2018).
35. Yi, M. et al. Symmetry-breaking orbital anisotropy observed for detwinned $BaFe_{1-x}Co_xAs_2$ above the spin density wave transition. *Proc. Natl Acad. Sci. USA* **108**, 6878–6883 (2011).
36. Kim, Y. et al. Electronic structure of detwinned $BaFe_2As_2$ from photoemission and first principles. *Phys. Rev. B* **83**, 64509 (2011).
37. Watson, M. D., Haghighirad, A. A., Rhodes, L. C., Hoesch, M. & Kim, T. K. Electronic anisotropies revealed by detwinned angle-resolved photo-emission spectroscopy measurements of FeSe. *New J. Phys.* **19**, 103021 (2017).
38. Pfau, H. et al. Detailed band structure of twinned and detwinned $BaFe_2As_2$ studied with angle-resolved photoemission spectroscopy. *Phys. Rev. B* **99**, 35118 (2019).
39. Riccò, S. et al. In situ strain tuning of the metal-insulator-transition of Ca_2RuO_4 in angle-resolved photoemission experiments. *Nat. Commun.* **9**, 4535 (2018).
40. Barber, M. E., Steppke, A., Mackenzie, A. P. & Hicks, C. W. Piezoelectric-based uniaxial pressure cell with integrated force and displacement sensors. *Rev. Sci. Instrum.* **90**, 23904 (2019).
41. He, M. et al. Dichotomy between in-plane magnetic susceptibility and resistivity anisotropies in extremely strained $BaFe_2As_2$. *Nat. Commun.* **8**, 504 (2017).
42. Hsu, Y.-T. et al. Manipulating superconductivity in ruthenates through Fermi surface engineering. *Phys. Rev. B* **94**, 45118 (2016).
43. Acharya, S. et al. Evening out the spin and charge parity to increase T_c in unconventional superconductors. *ArXiv Prepr*. https://arxiv.org/abs/181105143 (2018).
44. Ghamari, S., Lee, S.-S. & Kallin, C. Renormalization group analysis of a neck-narrowing Lifshitz transition in the presence of weak short-range interactions in two dimensions. *Phys. Rev. B* **92**, 85112 (2015).
45. Efremov, D. V. et al. Multicritical Fermi surface topological transitions. *ArXiv Prepr*. https://arxiv.org/abs/181013392 (2018).
46. Berg, E., Hartnoll, S. A. & Mousatov, C. H. Theory of strange metals from hot fermions. *ArXiv Prepr*. https://arxiv.org/abs/181012945 (2018).
47. Isobe, H. & Fu, L. Supermetal. *ArXiv Prepr*. https://arxiv.org/abs/190505188v1 (2019).
48. Paglione, J. et al. Elastic tensor of Sr_2RuO_4. *Phys. Rev. B* **65**, 220506 (2002).
49. Chu, J.-H., Kuo, H.-H., Analytis, J. G. & Fisher, I. R. Divergent nematic susceptibility in an iron arsenide superconductor. *Science* **337**, 710–712 (2012).
50. Bobowski, J. S. et al. Improved single-crystal growth of Sr_2RuO_4. *Condens. Matter* **4**, 6 (2019).
51. Hoesch, M. et al. A facility for the analysis of the electronic structures of solids and their surfaces by synchrotron radiation photoelectron spectroscopy. *Rev. Sci. Instrum.* **88**, 13106 (2017).
52. Koepernik, K. & Eschrig, H. Full-potential nonorthogonal local-orbital minimum-basis band-structure scheme. *Phys. Rev. B* **59**, 1743–1757 (1999).
53. Opahle, I., Koepernik, K. & Eschrig, H. Full-potential band-structure calculation of iron pyrite. *Phys. Rev. B* **60**, 14035–14041 (1999).
54. Perdew, J. P., Burke, K. & Ernzerhof, M. Generalized gradient approximation made simple. *Phys. Rev. Lett.* **77**, 3865–3868 (1996).
55. Eschrig, H., Richter, M. & Opahle, I. Relativistic solid state calculations. in *Relativistic Electronic Structure Theory, (Part II, Applications)*, (ed. Schwerdtfeger, P.), Vol. 13, 721 (Elsevier, Amsterdam, 2014).
56. Chmaissem, O., Jorgensen, J. D., Shaked, H., Ikeda, S. & Maeno, Y. Thermal expansion and compressibility of Sr_2RuO_4. *Phys. Rev. B* **57**, 5067–5070 (1998).